IEEE Open Journal of
Power Electronics

Received 4 June 2023; revised 27 July 2023; accepted 5 August 2023. Date of publication 11 August 2023;
date of current version 31 August 2023. The review of this article was arranged by Associate Editor Telles Brunelli Lazzarin.

Digital Object Identifier 10.1109/OJPEL.2023.3304279

Large- and Small-Signal Modeling Derived Loss Optimal Power Loop Decoupling Mechanism of TAB Converter

SAIKAT DEY (Graduate Student Member, IEEE), AND AYAN MALLIK (Senior Member, IEEE)

The Polytechnic School, Arizona State University, Mesa, AZ 85212 USA

CORRESPONDING AUTHOR: AYAN MALLIK (e-mail: ayan.mallik@asu.edu)

This work was partly supported by CoolCAD Electronics.

ABSTRACT This article presents a precisely synthesized full order as well as reduced order continuous time large signal and small signal model of a hybrid phase-duty controlled triple-active bridge (TAB) converter based on higher order harmonic frequency inclusive averaging model. Such model helps to accurately predict the steady state circuit parameters such as inductor current, average output voltage, output voltage ripple etc. that in turn can be used to formulate the loss minimized optimal phase-duty modulation strategy for a TAB. Further, the derived full order small signal model can specifically model the high frequency dynamics of the converter which are neglected in the reduced order modeling. Moreover, in order to facilitate decoupled power flow in a TAB, a decoupler network is formulated based on meticulously modeled converter plant considering higher order harmonics of the bridge voltages into calculation. Finally, a controller-based decoupled power management strategy is proposed in this study that decouples the TAB control loops and facilitates faster transient performance with two independent PI controllers. An 800 W TAB converter proof-of-concept is designed, fabricated, and tested to verify the established modeling techniques and the proposed controller decoupling action. With the implementation of the decoupled control under an 80% load transient at the 2nd output port, the experimental results show 30% improvement in overshoot compared to the fundamental harmonic based decoupling method.

INDEX TERMS Frequency selective small and large signal modeling, loss optimized decoupled control, triple-active-bridge (TAB).

I. INTRODUCTION

In cutting-edge applications such as electric-vehicle power train, space power supplies, smart/micro-grids wherever multiple energy resources (e.g., solar cells, wind energy, fuel cell, battery units, local loads etc.) are engaged together to efficiently support the power system, a power electronic converter that can control and direct the power flow with high performance, is needed [1], [2], [3]. Here, an isolated omni-directional multiport converter (MPC) that utilizes a single power stage to interconnect all the ports, instead of individual dc-dc stage, can be employed to simplify the design. One of the prominent circuit topologies among the multi-winding transformer coupled MPC family is multi-active bridge (MAB) converter, that has been first proposed in [3]. An n-port MAB converter is comprised of n full-bridge modules magnetically coupled through an n-winding high-frequency (HF) transformer as illustrated in Fig. 1. The reported applications of MAB converter are widespread from distributed space power supplies [4], [5], renewable generation systems [6], [7], EV on-board chargers [9] to more-electric aircraft power systems [10].

Owing to the inherent power flow cross-coupling problem, the primary research focus on the MAB converter design has been on decoupling the control loops [6], [11], [12], [13], [14], [15], [16] and to replace the complex multi-input-multi-output (MIMO) system with multiple independent single-input-single-output (SISO) control loops. Such decoupling techniques that are reported in literature, can be broadly

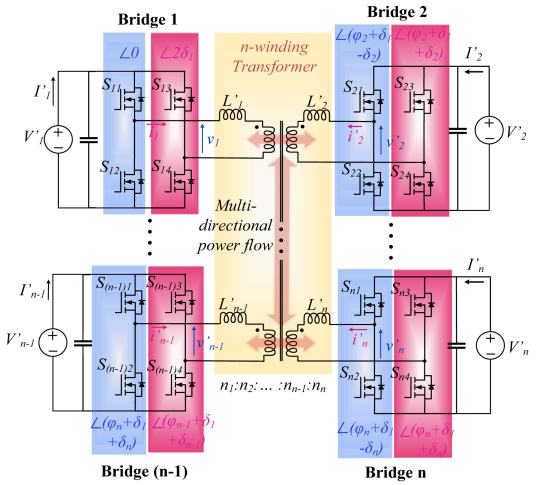

FIGURE 1. Generic n-port MAB converter topology and phase shifts of the respective half-bridge gating signals.

categorized into two methods: software-based and hardware-based. In software-based decoupling techniques [6], [11], [12], [13], modified control algorithms are employed in the controller in order to restrict the coupling effects of the TAB converter. The works in [6], [11] use different bandwidths for the SISO control loops to decouple them from one another. However, in this process, a control loop having maximum bandwidth can adequately attenuate the disturbance from other loops, but the loops with lower bandwidth will have deteriorated dynamic performance. Other such techniques use feedforward compensators, which dynamically decouples the power control loops with the help of decoupling matrices that are precomputed and stored as a look-up table in the controller [12]. In the work [12], the TAB converter is modeled using fundamental harmonic approximation (FHA) that leads to inaccurate calculation of the decoupling matrices; hence, it results in poor decoupling performance. Another method to route the matrix power flow in a MAB is time-sharing (TS) based control [13]. Although this DAB-like MAB control method solves the power coupling challenge and helps in achieving better light load efficiency, the MAB converter with TS-control strategy suffers from higher output voltage ripple, increased output capacitor sizing and reduced power rating of the ports.

In order to attain decoupled power transfer in a scalable MAB topology while avoiding complex controller implementation, a few hardware based decoupling approaches have been introduced in the literature [14], [15]. In the work presented in [14], the coupling between the MAB ports is eliminated by removing the leakage inductance from a master port, whereas similar decoupling approach adopted in [15] introduces a resonant capacitor in series with a port's leakage inductance to make the leakage impedance at fundamental frequency zero. However, such strategy requires a modified configuration of the MAB converter that annihilates the fundamental architectural symmetry of the topology and hence puts down the inherent design advantages of the converter. Also, by eliminating the equivalent impedance from a port of a MAB structure, the RMS and peak of that port's current increases considerably that incurs more conduction and switching losses.

Nevertheless, none of the reported literature on decoupling control of TAB or MAB, takes care of the increased system losses at the non-unity gain and light load conditions due to increased port current RMSs and peaks [4], [5]. The application of the optimal phase-duty control under power flow decoupling action is fairly non-existent in the literature. The authors in [16] made an effort to propose a universal solution to control the decoupled MAB power flow under minimum current point tracking (MCPT) algorithm in order to reduce the conduction loss but the implementation of power flow decoupling strategy is based on FHA model with compromised accuracy. The FHA based analysis misses out information about the current shapes and thus fails to precisely calculate the conduction as well as the switching loss of the converter, thus, leads to a non-loss-optimal point converter operation. Consideration of switching frequency harmonic components in the modeling of dual-active-bridge (DAB) converters can be found in [17]; however, no such approach is present for TAB and its accurate large and small signal model formulation. Therefore, through the present work, the authors precisely synthesize the required TAB winding current and output voltage information from a loss inclusive full-order average model (FOAM) that takes the higher order switching frequency harmonics into account as proposed in the article. In contrast to the FHA based FOAM, our modeling method results in higher estimation accuracy for the state-variables due to higher order harmonics under consideration, leading to the accurately optimized TAB modulation strategy. Furthermore, in order to decouple the power flow in such a TAB converter, a decoupling matrix is formulated in this work from the generalized-harmonic-approximated (GHA) plant model, which when cascaded with the plant, decouples the control loops. Further, a detailed GHA oriented small signal modeling of the TAB converter is also presented in this work that can be used while modeling the controller for the plant. Finally, a loss optimal decoupled TAB converter power flow management scheme is presented in this work. For validation purposes of the claims stated in the work, a triple active bridge (TAB) converter for space application is designed to be rated for 400 W at each of the output ports, where the input and output port voltages range between 160V, 90-140V, and 16-27V, respectively. The major contributions of the work can be briefed as follows:

1) The analytically developed GHA based generic model of the n-port MAB converter involving phase-duty-based multivariable control works as a building block for the development of the reduced order TAB plant model.
2) This article presents the FHA and GHA based full order as well as reduced order large signal and small signal continuous time modeling of the TAB converter along with their comparison with regard to the control parameters.

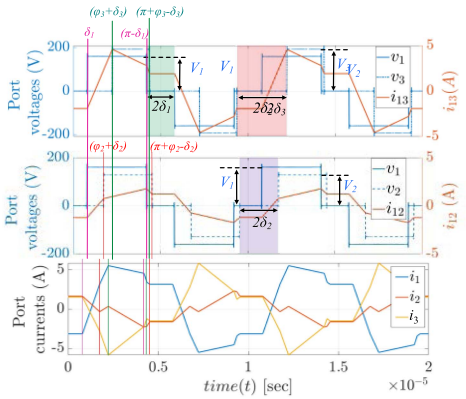

FIGURE 2. Typical TAB port voltage and current waveforms.

3) The power flow decoupling matrices are formulated (and implemented in the digital controller), based on the GHA based reduced order TAB circuit model, which reduces the settling time and overshoot by 3.5 folds and 3 folds, compared to the existing FHA based decoupling action, respectively.
4) Closed loop implementation of the proposed optimal-duty cycle control has been established in this work alongside the power loop decoupled controller.

II. GHA-BASED VOLTAGE WAVEFUNCTION AND POWER FLOW SYNTHESIS IN A MAB CONVERTER

To elucidate the operation and modeling of any converter power stage from the MAB family (including TAB), this section presents the frequency domain approach to accurately formulate the converter ports' voltage, current and power flow waveshapes for a generalized MAB converter. The topology of a generic n-port MAB converter is presented in Fig. 1, where **n** active full bridges are magnetically coupled through a multi-winding high-frequency transformer having a turns ratio of $n_1, n_2, \ldots n_n$. The corresponding dc link voltage and the leakage inductance of the transformer, connected to port-i ($1 \leq i \leq n$), are highlighted as V_i' and L_i'. The degrees of freedom to control the power flow in a MAB are defined by the bridge voltage duty ratios (δ_i) and the inter- bridge phase differences (φ_i, $\varphi_1 = 0$). The phase displacement between the gating signals of the two half-bridge (HB) legs of any particular AB controls the duty cycle of the bridge output voltage as shown in Figs. 1 and 2.

Due to the complexity in analyzing the power transfer between the MAB ports under phase-duty control using the time-domain MAB model, a GHA based frequency domain analysis is carried out in this article. Utilizing the Fourier series expansion, each of the quasi-square shaped ac bridge voltages (v'_i, for port-I H-bridge) can be expressed as a series combination of sinusoidal voltage sources of odd order harmonics and can be expressed as,

$$v'_i(t) = \frac{4V'_i}{\pi} \cdot \sum_{k=1,3,\ldots}^{\infty} \frac{1}{k} d_{ki} \sin\{k(\omega t - \varphi_i)\}, \tag{1}$$

where $d_{ki} = \cos(k\delta_i)$; 'k' is the order of the harmonic, and $\omega = 2\pi f_{sw}$; f_{sw} being the operating switching frequency.

The total power sourced by the any of the MAB port (port-i) can be quantified as the summation of the power transfers to the rest of the ports, as represented in (2).

$$P_i = \sum_{\substack{j=1 \\ j\neq i}}^{n} P_{ij} = \sum_{\substack{j=1 \\ j\neq i}}^{n} \frac{4V'_i V'_j}{\pi^3 f_{sw} L'_{ij}} \cdot \sum_{k=1,3,\ldots}^{\infty} \frac{1}{k^3} \left[d_{ki} d_{kj} \sin\{k(\varphi_i - \varphi_j)\} \right] \tag{2}$$

where φ_j and φ_i are the corresponding phase shifts; V_i and V_j are the dc link voltages, respectively and L_{ij} is the equivalent line inductance between the ports, given in (3).

$$L_{ij} = L_i + L_j + L_i L_j \left(\sum_{k\neq i,j}^{n} \frac{1}{L_k} \right); \; i \neq j. \tag{3}$$

Here, L_i and L_j represent the transformer leakage inductances of I and j-th ports referred to the port-1, respectively: $L_i = L'_i(\frac{n_i}{n_1})^2$; $L_j = L'_j(\frac{n_j}{n_1})^2$. The derivation of the GHA based generalized MAB power flow model is further employed later in this work in order to synthesize the GHA oriented reduced order model of the TAB converter under study as well as its decoupler network.

III. DERIVATION OF THE HARMONIC-INCLUSIVE AVERAGE MODEL (HIAM) OF TAB CONVERTER

In the quest to accurately estimate the transformer winding currents and their RMSs and further to develop an efficient decoupled closed loop controller for a TAB converter, precise synthesis of the converter's large signal as well small signal average models is extremely necessary. In this work, the generalized averaging technique [18] is employed to model the TAB converter, where the higher order switching frequency harmonic terms are included alongside the fundamental, in Fourier series of the state variables (HIAM). The existing fundamental component-oriented GAM models of DAB leads to an inaccurate steady state model of the converter due to exclusion of the higher order components. Whereas the proposed HIAM of TAB helps to predict the precise large signal as well as small signal disturbances in the system.

A. HARMONIC-INCLUSIVE FULL ORDER LARGE SIGNAL MODEL (HIFOAM) DEVELOPMENT

The derivation of the large signal state space model of the TAB converter starts from the Δ-equivalent model of the TAB, as highlighted in Fig. 3(a). Here, on-state resistances of the

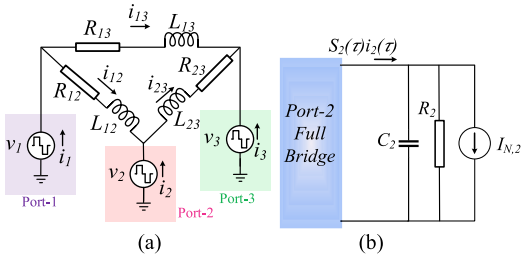

FIGURE 3. (a) Δ-equivalent model of the TAB converter with lumped winding resistances. (b) Example output Port Model in a TAB.

switching devices and the transformer winding resistances are lumped together (R_{12}, R_{23} and R_{13}) and are placed in series with the inter-port impedances. The time-varying ac quasi-square port voltages can be represented as:

$$v_1(\tau) = s_1(\tau)\, v_{in}(\tau) \tag{4}$$

$$v_2(\tau) = s_2(\tau)\, v_{o2}(\tau) \tag{5}$$

$$v_3(\tau) = s_3(\tau)\, v_{o3}(\tau) \tag{6}$$

where $v_{in}(\tau)$, $v_{o2}(\tau)$, and $v_{o3}(\tau)$ are the dc link port voltages and $s_1(\tau)$, $s_2(\tau)$, and $s_3(\tau)$ are the switching functions that depend on the phase-duty control variables and can be defined as given in (7) shown at the bottom of this page derived from the switching modulation scheme. , where i signifies a particular TAB port; $i = 1, 2,$ *or* 3 and $\omega = 2\pi f_{sw}$; f_{sw} being the switching frequency.

In this work, for the ease of modeling, the port-2 and port-3 of TAB converter are taken as output ports while port-1 works as an input to the system. Furthermore, the inter-port inductor currents of the Δ TAB circuit, i_{12}, i_{13} and i_{23}, and the output capacitor voltages v_{o2} and v_{o3} are selected as the primary state variables for the modeling purposes. Now, applying KVL and KCL in Fig. 3, the state equations of a TAB converter are obtained.

$$\frac{di_{12}(\tau)}{d\tau} = -\frac{R_{12}}{L_{12}} i_{12}(\tau) + \frac{s_1(\tau)\, v_{in}(\tau)}{L_{12}} - \frac{s_2(\tau)\, v_{o2}(\tau)}{L_{12}} \tag{8}$$

$$\frac{di_{13}(\tau)}{d\tau} = -\frac{R_{13}}{L_{13}} i_{13}(\tau) + \frac{s_1(\tau)\, v_{in}(\tau)}{L_{13}} - \frac{s_3(\tau)\, v_{o3}(\tau)}{L_{13}} \tag{9}$$

$$\frac{di_{23}(\tau)}{d\tau} = -\frac{R_{23}}{L_{23}} i_{23}(\tau) + \frac{s_2(\tau)\, v_{o2}(\tau)}{L_{23}} - \frac{s_3(\tau)\, v_{o3}(\tau)}{L_{23}} \tag{10}$$

$$\frac{dv_{o2}(\tau)}{d\tau} = -\frac{v_{o2}(\tau)}{R_2 C_2} + \frac{s_2(\tau)\, i_{12}(\tau)}{C_2} - \frac{s_2(\tau)\, i_{23}(\tau)}{C_2} - \frac{I_{N,2}(\tau)}{C_2} \tag{11}$$

$$\frac{dv_{o3}(\tau)}{d\tau} = -\frac{v_{o3}(\tau)}{R_3 C_3} + \frac{s_3(\tau)\, i_{13}(\tau)}{C_3} - \frac{s_3(\tau)\, i_{23}(\tau)}{C_3} - \frac{I_{N,3}(\tau)}{C_3}. \tag{12}$$

Where C_2, C_3 are the output dc link capacitances and $I_{N,2}(\tau)$, $I_{N,3}(\tau)$ are dc load currents.

Equations (8)–(12) are simultaneously time-varying and nonlinear in nature. In order to obtain the linear time-invariant model, the next step is to apply the averaging method by approximating each state variable, $x(\tau)$ as an exponential Fourier series.

$$x(\tau) = \sum_{k=-\infty}^{\infty} \langle x\rangle_k(\tau)\, e^{jk\omega_s \tau}, \tag{13}$$

where $\omega_s = \frac{2\pi}{T_s}$, and $\langle x\rangle_k$ is the k^{th} coefficient in the Fourier series that represents the amplitude of kth harmonic.

Similar to a conventional state-space average model, in the TAB model equivalent, few of the state variables such as the input and output voltages, v_{in}, v_{o2}, and v_{o3}, and load currents $I_{N,2}$, $I_{N,3}$ can be simplified using small ripple approximation, which means that only dc term in the Fourier series will remain. On the other hand, for the purely ac current state variables, i_{12}, i_{13} and i_{23}, need to be approximated by first k odd terms in their Fourier series due to the half-wave symmetry of their wavefunctions. Also, the state equations are expanded using the following relationships [21]:

$$\frac{d}{dt}\langle x\rangle_k = \left\langle \frac{d}{dt} x \right\rangle_k - jk\omega_s \langle x\rangle_k \tag{14}$$

$$\langle xy\rangle_k = \sum_{i=-\infty}^{\infty} \langle x\rangle_{k-i} \langle y\rangle_i \tag{15}$$

Applying (15), (16) to the state space equations in (8)–(12), the zeroth and 1st harmonic coefficients of i_{23} and only zeroth coefficient of v_{o2} can be determined as (16)–(19), shown at the bottom of next page. Same approach is taken for other state variables as well.

Now, applying the small ripple approximation criteria on the input and output side capacitor voltages, the following can be deduced: $\langle v_{in}\rangle_0 = V_1$, $\langle v_{in}\rangle_{kR} = \langle v_{in}\rangle_{kI} = 0$, $\langle v_{o2}\rangle_{kR} = \langle v_{o2}\rangle_{kI} = 0$, $\langle v_{o3}\rangle_{kR} = \langle v_{o3}\rangle_{kI} = 0$, where k is any odd switching frequency harmonic. On the other hand, the zeroth and higher order Fourier coefficients of purely ac switching functions are obtained as:

$$\langle s_1\rangle_0 = \langle s_2\rangle_0 = \langle s_3\rangle_0 = 0;$$

$$\langle s_2\rangle_{kR} = -\frac{2}{\pi k}\cos(k\delta_2)\sin(k\varphi_2);$$

$$\langle s_2\rangle_{kI} = -\frac{2}{\pi k}\cos(k\delta_2)\cos(k\varphi_2);$$

$$s_i(\tau) = \begin{cases} 1, & \frac{\delta_1+\varphi_i}{\omega} \le \tau \le \frac{\pi+\varphi_i-\delta_1}{\omega} \\ 0, & 0 \le \tau \le \frac{\delta_1+\varphi_i}{\omega};\ \frac{\varphi_i+\pi-\delta_1}{\omega} \le \tau \le \frac{\varphi_i+\pi+\delta_1}{\omega};\ \frac{2\pi+\varphi_i-\delta_1}{\omega} \le \tau \le \frac{2\pi}{\omega} \\ -1, & \frac{\varphi_i+\pi+\delta_1}{\omega} \le \tau \le \frac{2\pi+\varphi_i-\delta_1}{\omega} \end{cases} \tag{7}$$

$$\langle s_3\rangle_{kR} = -\frac{2}{\pi k}\cos(k\delta_3)\sin(k\varphi_3);$$
$$\langle s_3\rangle_{kI} = -\frac{2}{\pi k}\cos(k\delta_3)\cos(k\varphi_3).$$

Finally, by using the obtained coefficient values in the extended kth harmonic order state equations (similar to (16)–(19)), a final set of differential state equations is formed with two output capacitor voltages and 6k variables representing the first kth coefficients of the three inter port inductor currents as the complete state variables. Thus, the state-space matrix of the TAB converter is formulated and shown in (20) shown at the bottom of this page. where, $X = [v_{o2}\ v_{o3}\ i_{12_{kR}}\ i_{12kI}\ i_{13kR}\ i_{13kI}\ i_{23kR}\ i_{23kI}]^T$;

A is a 8×8 matrix that can be represented as $\begin{bmatrix} a_{11}\ldots a_{18} \\ \vdots\ \ddots\ \vdots \\ a_{81}\ldots a_{88} \end{bmatrix}$; M is a 3×8 matrix that can be represented as $\begin{bmatrix} M_{11}\ldots M_{13} \\ \vdots\ \ddots\ \vdots \\ M_{81}\ldots M_{83} \end{bmatrix}$ and $N = [v_{in}\ I_{N,2}\ I_{N,3}]^T$. The individual terms of the state-space matrix are highlighted in the appendix section.

The steady state large-signal values of the state variables such as output port voltages and transformer winding currents can be obtained by solving $\dot{X} = 0$. In order to validate the effectiveness of the formulated large signal GHA oriented averaging model over the FHA based model, the variations in steady state TAB output voltages for both the modeling approaches are plotted in Figs. 4 and 5 with a wide sweep in φ_2. The modeling errors from the GHA and FHA oriented average models with respect to the experimentally evaluated data are also presented in the plots. It can be inferred from both the plots that the large signal TAB model considering up to 5th order harmonic provides an average of 4% better accuracy than the conventional FHA based full order model, which in turn facilitates the improved and precise estimation of the converter steady state parameters depending on the phase-duty control variables. Please note that the TAB circuit parameters as per the model developed and experiments conducted are given in Table 1. Moreover, such precisely quantified large signal steady state model helps obtaining the optimal duty cycle parameters depending on the output gain and load condition through TAB loss optimization framework, discussed in [3], [4].

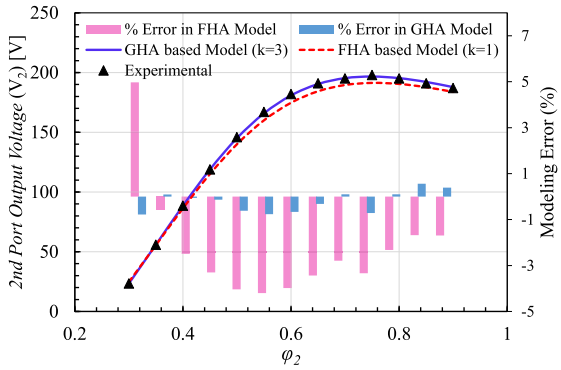

FIGURE 4. Comparison of experimental and estimated port-2 dc voltage, derived from FHA and GHA based Full Order TAB model with a variation in φ_2.

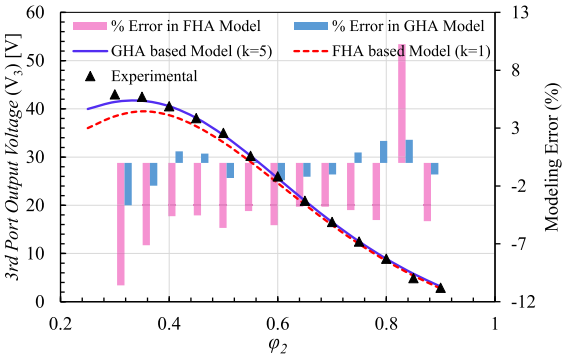

FIGURE 5. Comparison of experimental and estimated port-3 dc voltage, derived from FHA and GHA based Full Order TAB model with a variation in φ_2.

$$\frac{d\langle i_{23}\rangle_0}{dt} = -\frac{R_{23}}{L_{23}}\langle i_{23}\rangle_0 + \frac{\langle s_2\rangle_0\langle v_{o2}\rangle_0}{L_{23}} + \frac{2}{L_{23}}\langle s_2\rangle_{1R}\langle v_{o2}\rangle_{1R} + \frac{2}{L_{23}}\langle s_2\rangle_{1I}\langle v_{o2}\rangle_{1I} - \frac{\langle s_3\rangle_0\langle v_{o3}\rangle_0}{L_{23}} - \frac{2}{L_{23}}\langle s_3\rangle_{1R}\langle v_{o3}\rangle_{1R} - \frac{2}{L_{23}}\langle s_3\rangle_{1I}\langle v_{o3}\rangle_{1I} \tag{16}$$

$$\frac{d\langle i_{23}\rangle_{1R}}{dt} = -\frac{R_{23}}{L_{23}}\langle i_{23}\rangle_{1R} + \omega_s\langle i_{23}\rangle_{1I} + \frac{1}{L_{23}}\left(\langle s_2\rangle_0\langle v_{o2}\rangle_{1R} + \langle s_2\rangle_{1R}\langle v_{o2}\rangle_0\right) - \frac{1}{L_{23}}\left(\langle s_3\rangle_0\langle v_{o3}\rangle_{1R} + \langle s_3\rangle_{1R}\langle v_{o3}\rangle_0\right) \tag{17}$$

$$\frac{d\langle i_{23}\rangle_{1I}}{dt} = -\frac{R_{23}}{L_{23}}\langle i_{23}\rangle_{1I} - \omega_s\langle i_{23}\rangle_{1R} + \frac{1}{L_{23}}\left(\langle s_2\rangle_0\langle v_{o2}\rangle_{1I} + \langle s_2\rangle_{1I}\langle v_{o2}\rangle_0\right) - \frac{1}{L_{23}}\left(\langle s_3\rangle_0\langle v_{o3}\rangle_{1I} + \langle s_3\rangle_{1I}\langle v_{o3}\rangle_0\right) \tag{18}$$

$$\frac{d\langle v_{o2}\rangle_0}{dt} = -\frac{1}{R_2C_2}\langle v_{o2}\rangle_0 + \frac{1}{C_2}\langle s_2\rangle_0\langle i_{12}\rangle_0 + \frac{2}{C_2}\left(\langle s_2\rangle_{1R}\langle i_{12}\rangle_{1R} + \langle s_2\rangle_{1I}\langle i_{12}\rangle_{1I}\right) - \frac{2}{C_2}\left(\langle s_2\rangle_{1R}\langle i_{23}\rangle_{1R} + \langle s_2\rangle_{1I}\langle i_{23}\rangle_{1I}\right) \tag{19}$$

$$\dot{X} = AX + MN \tag{20}$$

TABLE 1. TAB Circuit Parameters

Circuit Parameters	*Values*
Input DC voltage (V_1)	160V
Secondary Output Port Voltage (V_2)	100-140V, 120V(nominal)
Secondary Output Port Rated Power (P_2)	400W
Tertiary Output Port Voltage (V_3)	16-28V, 22V(nominal)
Tertiary Output Port Rated Power (P_3)	400W
Transformer Turns Ratio (N_1, N_2, N_3)	7:5:1
Magnetizing Inductance (L_m)	300μH
Total Leakage Inductances (L_1, L_2', L_3')	16μH, 15μH, 0.28 μH
Secondary side Output Capacitor (C_2)	86μF
Tertiary Output Capacitor (C_3)	47μF
Switching frequency (f_{sw})	100 kHz

B. FULL ORDER SMALL SIGNAL AVERAGE MODEL DEVELOPMENT

In order to design a controller for the TAB converter and also, to perform dynamic stability analysis, the derivation of small-signal control-to-output transfer functions are necessary. In (20), when there is a small perturbation in the phase shift control variables φ_2 and φ_3, the state variables of $[X]$ will deviate from their steady state operating points. Although the duty variables of a TAB are varied in steady state to achieve lesser conduction and switching losses [3], the converter output voltage or current or power is regulated by controlling the phase-shift variables using some robust PI based controller and the dynamics of the duty cycle variables are much slower (∼100-1000 times) than the phase shift variables. Therefore, in this article, while deriving the small signal model, the perturbations in the duty cycle variables δ_2 and δ_3 are neglected. Hence, the deviations of the state variables are defined as,

$$\begin{aligned}
\Delta\varphi_2 &= \varphi_2 - \phi_2;\\
\Delta\varphi_3 &= \varphi_3 - \phi_3;\\
\Delta v_{o2} &= v_{o2} - V_{o2};\\
\Delta v_{o3} &= v_{o3} - V_{o3};\\
\Delta i_{ij_{kR}} &= i_{ij_{kR}} - I_{ij_{kR}};\\
\Delta i_{ij_{kI}} &= i_{ij_{kI}} - I_{ij_{kI}}
\end{aligned} \tag{21}$$

Where i, j = 1, 2, or 3; i ≠ j. Here, the upper-case variables depict steady state values while the lower-case and Δ variables present the large-signal and small-signal states, respectively.

Equation (20) contains nonlinear terms with multiplication of state variables with control inputs. Such a term $\sin(k\varphi_3)v_{o2}$, under small $\Delta\varphi_3$, can be approximated using (22).

$$\begin{aligned}
v_{o2}\sin(k\varphi_3) &= \sin\{k(\Delta\varphi_3+\phi_3)\}(\Delta v_{o2}+V_{o2})\\
&= V_{o2}\sin(k\phi_3) + V_{o2}\cos(k\phi_3)\,k\Delta\varphi_3 + \Delta v_{o2}\sin(k\phi_3)
\end{aligned} \tag{22}$$

In a similar fashion, all the nonlinear terms can be also approximated.

The HIFOAM based (approximated up to kth order harmonic) small-signal model of the TAB converter can thus be determined by substituting equations of (21) in (20) and is given in (23) as a form of a matrix equation.

$$\dot{x} = Ax + B\varphi. \tag{23}$$

Where, $x = [\Delta v_{o2}\ \Delta v_{o3}\ \Delta i_{12_{kR}}\ \Delta i_{12kI}\ \Delta i_{13kR}\Delta i_{13kI}\Delta i_{23kR}\ \Delta i_{23kI}]^T$;

$\varphi = [\Delta\varphi_2\ \Delta\varphi_3]^T$; $B = [B_1\ B_2\ B_3\ B_4\ B_5\ B_6\ B_7\ B_8]^T$;

$$B_1 = \left[-\sum\frac{4d_{k2}}{\pi C_2}\{i_{2kR}\cos(k\varphi_2) - i_{2kI}sin(k\varphi_2)\}\ \ 0\right];$$

$$B_2 = \left[0\ \ -\sum\frac{4d_{k2}}{\pi C_3}\{i_{3kR}\cos(k\varphi_3) - i_{3kI}sin(k\varphi_3)\}\right];$$

$$B_3 = \left[\frac{2V_2d_{k2}\cos(k\varphi_2)}{\pi L_{12}}\ \ 0\right];\ B_4 = \left[\frac{2V_2d_2\sin(k\varphi_2)}{\pi L_{12}}\ \ 0\right];$$

$$B_5 = \left[0\ \ \frac{2V_3d_{k3}\cos(k\varphi_3)}{\pi L_{13}}\right];\ B_6 = \left[0\ \ -\frac{2V_3d_{k3}\sin(k\varphi_3)}{\pi L_{13}}\right];$$

$$B_7 = \left[-\frac{2V_2d_{k2}\cos(k\varphi_2)}{\pi L_{23}}\ \ \frac{2V_3d_{k3}\cos(k\varphi_3)}{\pi L_{23}}\right];$$

$$B_8 = \left[\frac{2V_2d_{k2}\sin(k\varphi_2)}{\pi L_{23}}\ \ -\frac{2V_3d_{k3}\sin(k\varphi_3)}{\pi L_{23}}\right].$$

From (23), the control-to-output transfer functions can be obtained as,

$$x(s) = M(s)\,\varphi(s), \tag{24}$$

where M is a matrix of {(2+6n) × 2} size and can be obtained as $M = (sI - A)^{-1}B$; n = number of harmonics accounted under GHA consideration.

Therefore, the control-to-output voltage gains can be calculated by (25) and (26).

$$\Delta v_{o2} = M_{11}\Delta\varphi_2 + M_{12}\Delta\varphi_3. \tag{25}$$

$$\Delta v_{o3} = M_{21}\Delta\varphi_2 + M_{22}\Delta\varphi_3. \tag{26}$$

It is clear from (25) and (26) that any disturbance in the phase shift of any individual port will simultaneously affect the output voltages of both the ports. Such cross-coupling between the TAB ports demands the development of the decoupled control loops.

C. REDUCED ORDER AVERAGE MODEL DEVELOPMENT

While the previously obtained full order model helps to accurately predict the steady state dynamics of the converter, a higher order harmonic-inclusive reduced order average model (HIROAM) is also derived in the article in order to model the TAB plant and its decoupling network with less computational complexity and hence implementation simplicity. The prime applicability of the HIROAM has been to design and digitally implement the decoupled control mechanism, presented in the following section, whereas the previously derived HIFOAM is employed to build the loss optimal multi-variable (hybrid phase-duty control, see [5]) control that ensures the maximum efficiency tracking of the converter for wide load and gain range. In such reduced order continuous time modeling, the

high frequency leakage inductor dynamics of the transformer is neglected [14] and only low frequency output capacitor dynamics are modeled.

In this study, sufficient effort has been put forward to derive a precise model of the TAB plant by taking higher order harmonics into account while involving the bridge voltage duty variables in the control system. The derivation of HIROAM begins with the GHA based quantified power flow calculations that are shown in Section II with an example of a n-port generic MAB. Using the port power equation, given in (2), the dc output port current of ith port in a n-port MAB converter can be obtained as

$$I_i = \frac{P_i}{V_i} = \sum_{\substack{j=1 \\ j\neq i}}^{n} \frac{4V_j}{\pi^3 f_{sw} L_{ij}} \cdot \sum_{k=1,3,\ldots}^{\infty} \frac{1}{k^3} \left[d_{ki} d_{kj} \sin\{k(\varphi_j - \varphi_i)\} \right]. \tag{27}$$

The Taylor series of the above port current I_i around a dc operating point I_i^* is,

$$I_i = I_i^* + \Delta I_i^* = \sum_{\substack{j=1 \\ j\neq i}}^{n} \sum_{k=1,3,\ldots}^{\infty} M^*_{\mathrm{i,j,k}} \sin\{k(\varphi_i - \varphi_j)\} + \sum_{\substack{j=1 \\ j\neq i}}^{n} \sum_{k=1,3,\ldots}^{\infty} kM^*_{\mathrm{i,j,k}} \cos\{k(\varphi_i - \varphi_j)\} \left(\Delta\varphi_i - \Delta\varphi_j\right), \tag{28}$$

where $M^*_{\mathrm{i,j,k}} = \frac{4V_j}{\pi^3 f_{sw} L_{ij}} \cdot \frac{d_{ki} d_{kj}}{k^3}$.

Thus, the small signal variation in I_i, ΔI_i^* can be modeled as (29).

$$\Delta I_i^* = \sum_{\substack{j=1 \\ j\neq i}}^{n} \sum_{k=1,3,\ldots}^{\infty} G_{ij,k} \Delta\varphi_i, \tag{29}$$

where $G_{ij} = -\sum_{\substack{j=1 \\ j\neq i}}^{n} \sum_{k=1,3,\ldots}^{\infty} kM^*_{\mathrm{i,j,k}} \cos\{k(\varphi_i - \varphi_j)\}$.

Applying the modeling method to a TAB converter, the output port current disturbances caused by the perturbation in phase shift variables can also be modeled and the small signal transfer function matrix of the converter is expressed in (30).

$$\Delta \mathrm{I} = \begin{bmatrix} \Delta I_2 \\ \Delta I_3 \end{bmatrix} = \begin{bmatrix} G_{22,k} & G_{23,k} \\ G_{32,k} & G_{33,k} \end{bmatrix} \begin{bmatrix} \Delta\varphi_2 \\ \Delta\varphi_3 \end{bmatrix} = \mathrm{G_k} \Delta\phi. \tag{30}$$

As predicted from the HIFOAM, the cross-coupled interaction between the control variables and the outputs are also observed from this HIROAM. Moreover, it is to be noted

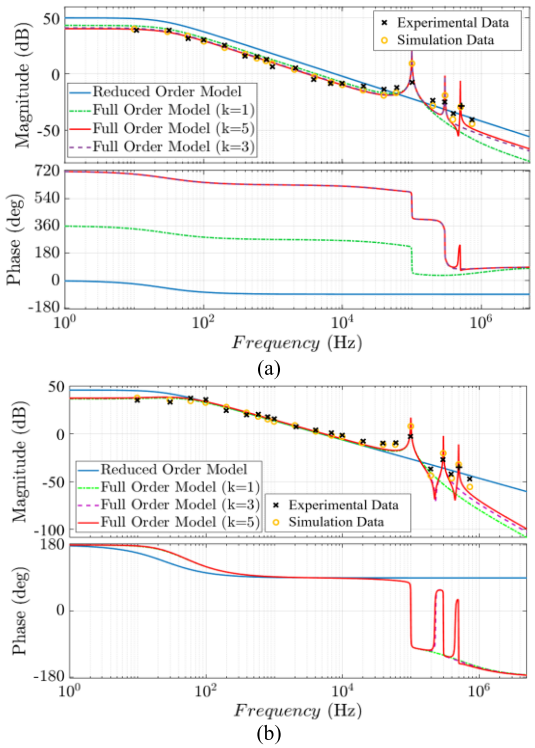

FIGURE 6. Calculated control-to-output gains by different modeling approaches, simulation, and experimentally measured data: (a) $\frac{\Delta v_{o2}}{\Delta \varphi_2}$; (b) $\frac{\Delta v_{o2}}{\Delta \varphi_3}$.

that the GHA based modeling (up to 5th order) of the plant helps in gaining a maximum of 7% better accuracy than the conventional FHA based reduced order modeling of the TAB converter.

To compare the above discussed full order and reduced order continuous time small signal models of the TAB topology, the port-2 output voltage, v_{o2}-to-port-2 phase shift (φ_2) and port-2 output voltage, v_{o2}-to-port-3 phase shift (φ_3) transfer functions obtained from various modeling techniques are graphically presented in Fig. 6(a) and (b), respectively. The accuracy of the developed models is assessed by measuring the control-to-output transfer functions of the TAB dc-dc converter through both MATLAB Simulink-based simulation and experimental approaches. To measure the control-to-output transfer function, a sinusoidal perturbation signal with a varying frequency (f_{pert}) is superimposed on the steady-state phase-shift control variables of port-2 (φ_2) and port-3 (φ_3) separately. The resulting superimposed phase-shift is fed to the PWM generator, which controls the switching devices in the power stage of the converter. The magnitude of the perturbation signal ($\Delta\varphi_2$ or $\Delta\varphi_3$) is set to 0.02, regardless of the value of f_{pert}. During the study, the perturbations in the output voltages of the TAB converter are recorded at each f_{pert} through an FFT analysis on the measured data. The control-to-output gain at f_{pert} is calculated using the formula $Gain = 20\log_{10}(\frac{\Delta v_{o2}}{\Delta \varphi_2})$ or $20\log_{10}(\frac{\Delta v_{o2}}{\Delta \varphi_3})$ with $\Delta\varphi_2$, $\Delta\varphi_3 = 0.02$. The simulation and experimental results of the

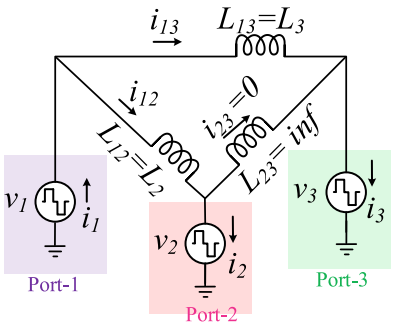

FIGURE 7. Δ-equivalent circuit of the TAB converter with zero leakage inductance of the transformer associated with port-1.

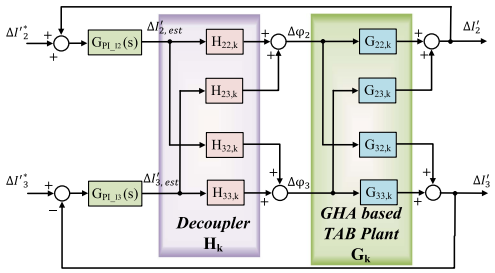

FIGURE 8. TAB converter plant and decoupled control system block diagram.

control-to-output transfer functions are presented in Fig. 6. The comparison between the calculated and measured transfer functions indicates a close match, demonstrating the accuracy of the developed models. However, some discrepancies are observed in between the reduced-order continuous-time model and the measured results. In contrast, the proposed higher order harmonic-inclusive full-order continuous-time model provides more accurate results, especially at the low and high-frequency zones. This finding further validates the accuracy of the formulated small-signal model of the converter. Thus, in this article, the derived full order small signal model is used to design the controller parameters of the TAB converter for better precision.

IV. LOSS MINIMIZED POWER FLOW LOOP DECOUPLING MECHANISM AND ITS DIGITAL IMPLEMENTATION

In order to obtain a robust and strict dynamic performance in a TAB converter, decoupling the control loops is necessary. An obvious approach to perform this task is to make leakage inductance of a transformer winding (of master port) near zero [14]. This phenomenon can be well understood if we deduce the equivalent circuits of the TAB network with line/leakage inductance associated with input port-1 (master port) to be zero, i.e., $L_1 = 0$, as shown in Fig. 7. In such scenario, the inter-port line inductances in Δ-equivalent circuit becomes, $L_{12} = L_2$, $L_{13} = L_3$ and $L_{23} = \infty$ (using (3)). This means no power can be transferred between the output ports: port-2 and port-3. Hence, the power sunk at port-2 and port-3 can be obtained from (2), as highlighted in (31).

$$P_2 = P_{12} + P_{32} = \sum_{\substack{j=1 \\ j\neq i}}^{n} \frac{4V'_1V'_2}{\pi^3 f_{sw}L_2} \cdot \sum_{k=1,3,\ldots}^{\infty} \frac{1}{k^3}\left[d_{k1}d_{k2}\sin\{k(\varphi_1-\varphi_2)\}\right];$$

$$P_3 = P_{13} + P_{23} = \sum_{\substack{j=1 \\ j\neq i}}^{n} \frac{4V'_1V'_3}{\pi^3 f_{sw}L_3} \cdot \sum_{k=1,3,\ldots}^{\infty} \frac{1}{k^3}\left[d_{k1}d_{k3}\sin\{k(\varphi_1-\varphi_3)\}\right] \quad (31)$$

It is evident from (31) that the individual power flow to the output ports is decoupled from each other, i.e., P_3 does not depend on φ_2 and P_2 does not depend on φ_3. In this way a DAB-like power flow can be achieved between the TAB master port and any other existing port in the system. However, this approach has a few drawbacks. First, obtaining a zero-leakage transformer is practically not feasible. Third, as the leakage inductance of a TAB port is reduced, it makes the converter more lossy with an increase in total winding RMS currents. Therefore, a controller based decoupling approach is adopted in this work while maintaining the minimal conduction loss operating point [4] by employing the duty cycle control variables.

A decoupling matrix, H is formulated in this work based on the HIROAM of TAB, as observed in (32), which decouples the control loops when placed in cascade with the converter plant $\mathbf{G_k}$. The previously derived HIFOAM is not utilized here in order to circumvent the computational complexity of the decoupling matrix elements, which is done online by the controller. While there are some loop decoupling control-based works reported in the literature [6], [11], [12], [13], their limitations are as follows: (a) loop transfer functions are formulated using FHA-based approximation by ignoring the higher order harmonics effect, while this assumption will often fail due to non-sinusoidal nature of the bridge voltages and currents, (b) the existing decoupled control schemes for a TAB converter fails to optimally adjust the bridge voltage duty cycles for a wide gain and load range operation, which is essential in order to achieve better system efficiency by minimizing the conduction as well as switching losses.

The proposed decoupled control system of the converter is depicted in Fig. 8. The focus of the decoupling network is to decompose the MIMO control system of a TAB into two separate independent SISO systems. Thus, the whole system can be controlled using independent non-interactive loop controllers, $G_{PI_{I_2}}(s)$ and $G_{PI_{I_3}}(s)$. The PI controllers are derived

while maintaining sufficient bandwidth and phase margin of the closed loop control system, derived from the full-order small signal model of the TAB. To achieve complete decoupling of the control loops, the H matrix is obtained as,

$$\mathrm{H_k} = \begin{bmatrix} H_{22,k} & H_{23,k} \\ H_{32,k} & H_{33,k} \end{bmatrix} = G_k^{-1} = \begin{bmatrix} G_{22,k} & G_{23,k} \\ G_{32,k} & G_{33,k} \end{bmatrix}^{-1} = \frac{1}{G_{11,k}G_{22,k} - G_{12,k}G_{21,k}} \begin{bmatrix} G_{22,k} & -G_{23,k} \\ -G_{32,k} & G_{33,k} \end{bmatrix}. \quad (32)$$

For every optimum operating point, the small signal transfer function matrix of the converter is only a constant, i.e., no pole or zero is involved since the inductor dynamics are already neglected, and so does the decoupling network $\mathrm{H_k}$, which is the inverse matrix of $\mathrm{G_k}$.

Additionally, to achieve optimal phase-duty control in the TAB dc-dc converter, the authors have previously presented a mathematical framework for a multivariable multi-constrained loss optimization problem [4], [5]. The objective function in this work aims to minimize the total loss, encompassing both conduction and switching losses in the switching network of the TAB, consisting of three full-bridge cells. The winding RMS currents that equivalently relate to the conduction loss in the system, are quantified from the previously derived loss-inclusive large-signal model of the TAB, whereas the obtained instantaneous switching currents are used in the switching loss calculation while accounting for the soft-switching events [5].

By optimizing the objective function based on specific design inputs, such as converter circuit parameters, output port voltage gains ($m_2 = \frac{V_2}{V_1}, m_3 = \frac{V_3}{V_1}$), and load requirements (P_2, P_3), the optimal set of phase and duty control variables (δ_k^*, φ_k^*) can be accurately derived. For a DAB converter, this optimization program can be solved offline using numerical optimization tools, and the obtained control variable set can be stored as a look-up table (LUT) in the controller. However, for a TAB, due to its complexity, the size of the LUT would become excessively large, leading to memory allocation challenges on the DSP. In this work, addressing a TAB converter, the authors have developed polynomial regression-based models for the optimal duty cycle control variables [18]. These models can be easily implemented within the DSP to achieve the desired control variables in real-time, considering the online load and voltage gain conditions of the TAB ports.

To formulate these optimal duty cycle calculation models, the loss optimization routine from [5] is executed to calculate the optimal control variable sets for various combinations of discrete gain and load values of the TAB converter ports. This data is then used to create a seven-column matrix ($m_2, m_3, P_2, P_3, \delta_1, \delta_2, \delta_3$) containing the TAB port gain, load, and the corresponding optimal duty cycle variables. Applying the least-mean-square method to this dataset, the authors statistically formulate the regression models for the optimal duty variables (δ_k), where δ_k is expressed as a polynomial function of the TAB ports' voltage gain and load condition: $\delta_k^* = \sum_{i=2}^{3} a_k m_i + b_k P_i + c_k m_i^2 + d_k P_i^2 + C_k$, where $k \in [1, 3], i \in [2, 3]$ a_k, b_k, c_k, d_k are the system coefficients and C_k is a constant. These models, expressed as second-order polynomial functions of the TAB ports' voltage gain and load condition, yield median errors of 4%, 5.2%, and 4.3% compared to the actual optimal δ_1, $\delta_2$and δ_3 datasets, respectively. Such precise models can be easily established inside the DSP without experiencing any memory allocation-based challenges. Thus, with the sensed output voltages and currents, the controller can update the bridge duty cycles online.

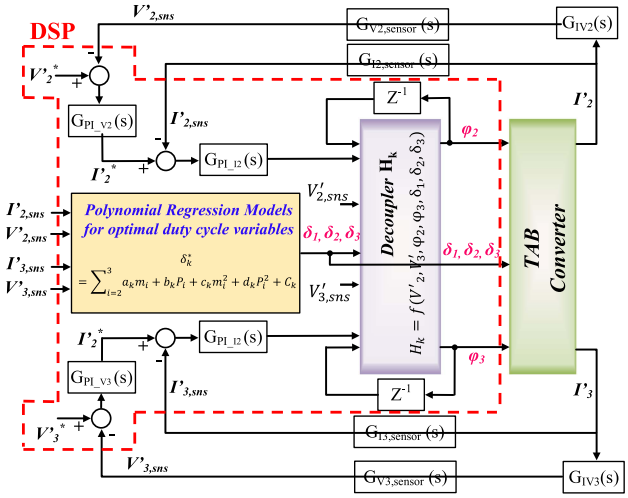

FIGURE 9. Implemented complete control system block diagram in the TAB converter under study.

In closed-loop implementation (Fig. 9), standalone PI controllers are utilized to track referenced output voltages or currents by dynamically adjusting the phase shift control parameters (φ_2, φ_3), while the duty-cycle parameters are updated using the optimal duty regression models to ensure maximum efficiency operation. The update rate of the optimal duty cycle block is maintained significantly slower (over 1000 times) than the time constant of the inbuilt PI controller, which modulates the phase shifts (φ_2, φ_3) dynamically. Consequently, any change in the operating duty cycle has a negligible effect on the output currents or voltages.

Moreover, based on sensed output voltages, online calculated optimal duty cycle control variables, and the phase shift variables from the previous cycle, the elements of the decoupling matrix $\mathrm{H_k}$ can be calculated and updated online within the controller. Additionally, the implemented decoupling matrix formulation accounts for up to the 5th order harmonics, providing better decoupling compared to when $\mathrm{H_k}$ is derived based on the conventional FHA-based plant model.

V. SIMULATION AND EXPERIMENTAL RESULTS

This section presents the simulation and experimental validation and benchmarking of the proposed decoupled power flow management in an 800 W TAB converter. The major circuit parameters of the converter under test are depicted in Table 1. The simulation study is carried out in MATLAB/Simulink

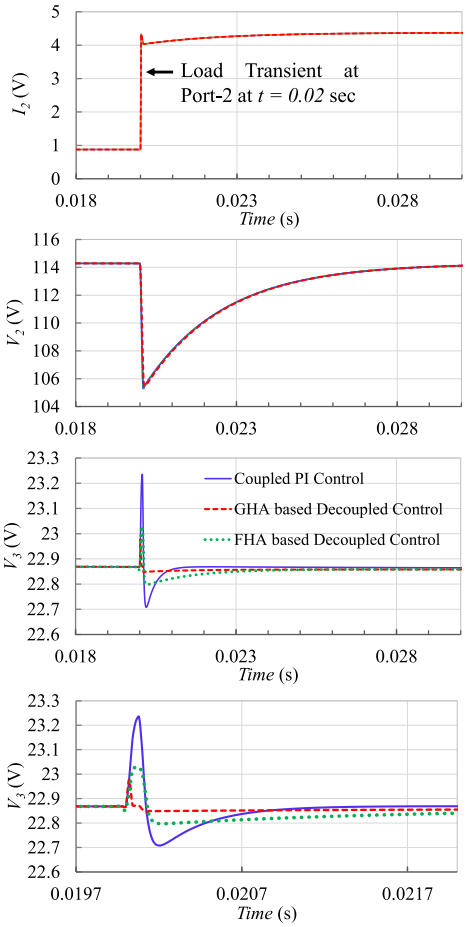

FIGURE 10. Transient response of TAB port voltages under step load at Port 2.

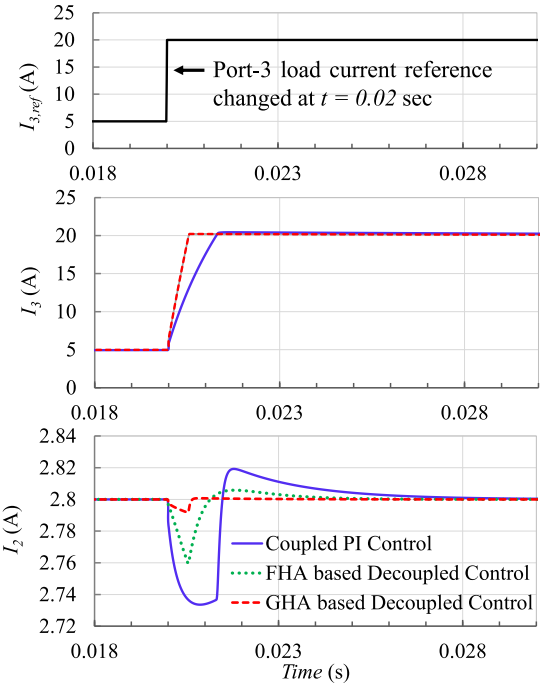

FIGURE 11. Transient response of TAB port currents under current reference change at Port 3.

simulation package. The port-1 of the TAB is used as the input port and the input voltage is kept constant at 160V, whereas the port-2 and port-3 are connected to resistive loads delivering power at voltage levels of 114V and 23V, respectively, as per the specification requirements in space-shuttle power conversion [20]. In the designed control system, two control loops are used to regulate the two output voltages. Phase shift control coupled with the optimal duty cycle control is used to control the power flow in the system. The PI controller for the voltage loop is designed to be of a lower bandwidth and hence slower than the inner current loops. For the current controller a crossover frequency of 1.2 kHz is selected, whereas the voltage controller bandwidth is kept as 12 Hz, which is, however, adjustable with the selection of controller coefficients. The decoupling matrix is calculated while considering up to 5th order harmonic and the parameters are obtained online based on the converter operating point.

In order to verify the usefulness of the proposed decoupling technique, two simulation cases are considered, and the results are summarized in Figs. 10 and 11.

1) Case-1 (Fig. 10): A load step is provided to the Port-2 load by reducing the port-2 load resistor value from 120 Ω to 27 Ω at t = 0.02 sec. Under this experiment, the voltage regulation of port-3 is kept under observation. For a comparative analysis, this same experiment is carried out with FHA and GHA based quantification of the H_k matrix. Also, the same controller's performance is tested in the absence of the decoupling network. The results, presented in Fig. 13, show that in case of coupled plant, such load transient in port-2 results in maximum overshoot of 0.5 V at port-3 capacitor voltage. This overshoot decreases by a significant margin once the decupling matrix is introduced in series with the TAB plant. Moreover, under the application of the GHA (k = 5) based decoupler, the overshot reduces by 23% compared to the FHA based decoupler. Also, the settling time reduces by 41% with as higher harmonics are modeled in the H_k formulation.
2) Case-2 (Fig. 11): Under this case, the TAB converter's output currents are regulated at certain values while the outputs are connected to dc battery loads. A change in port-3 output current reference is imposed on the control system at t = 0.02 sec to observe its effect on the port-2 current regulation. It can be inferred from the simulation results that the port-2 current experiences a disturbance of 2.85 % when there is no decoupling strategy involved. However, after applying the FHA and GHA based decoupling, this disturbance reduces by 56% and 78%, respectively. Further, the settling time of the current disturbance is reduced by 39% after application of the GHA based decoupling over the FHA method.

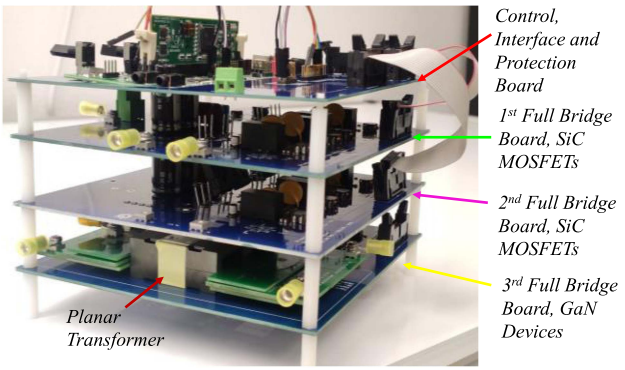

FIGURE 12. Triple Active Bridge (TAB) dc–dc converter prototype.

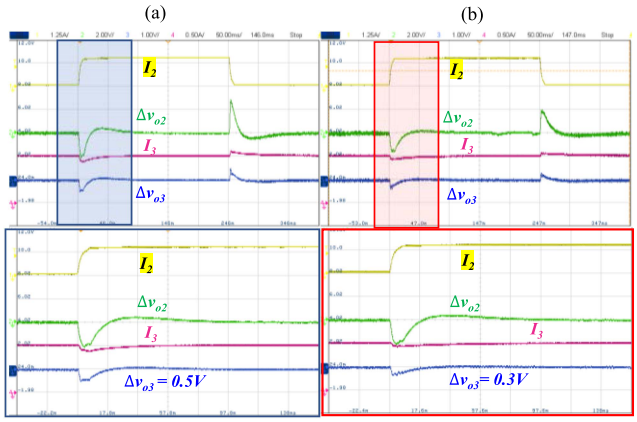

FIGURE 13. Experimental dynamic behavior of the TAB output ports under different decoupling actions due to 80% load transient in Port-2: (a) FHA based decoupling; (b) GHA based decoupling. Scale: I_2 (ch 1, dc coupled): 1.25 A/div; I_3 (ch 3, dc coupled): 0.5 A/div; V_{o2} (ch 2, ac coupled): 2 V/div; V_{o3} (ch 4, ac coupled): 1 V/div.

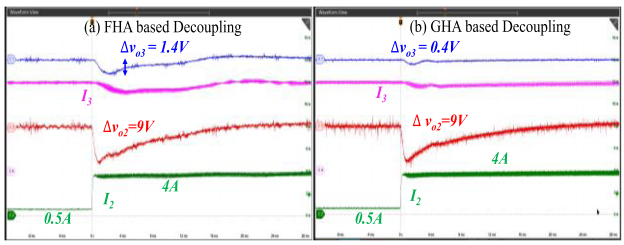

FIGURE 14. Experimental dynamic behavior of the TAB output ports under different decoupling actions due to load transient in Port-2 from 60 W to 500 W while Port-3 is connected to a constant 400 W load: (a) FHA based decoupling; (b) GHA based decoupling. Scale: I_2 (ch 2, dc coupled): 2 A/div; I_3 (ch 4, dc coupled): 2 A/div; V_{o2} (ch 3, ac coupled): 5 V/div; V_{o3} (ch 1, ac coupled): 2 V/div; time: 4 ms/div.

These simulation results validate the effectiveness of implementing a decoupling network computed using GHA method to reflect the impact of higher order harmonics modeling on the system dynamic performance.

Experiments on the laboratory proof-of-concept of the TAB converter are also performed to showcase performance of the decoupled control strategy. The converter prototype with major circuit components is highlighted in Fig. 12. The major circuit parameters of the converter under the test are depicted in Table 1. The port-1 of the TAB is used as the input port and the input voltage is kept constant at 160V, whereas the port-2 and port-3 are connected to resistive loads delivering power at voltage levels of 114V and 23V, respectively. Further, a three winding planar transformer is employed to couple all the three ports that has a turns ratio of 7:5:1.c The central controller is implemented on a Texas Instruments TMS320F28379D DSP. The PI controller for the voltage loop is designed to be of a lower bandwidth and hence slower than the inner current loops. For the current controller a crossover frequency of 1.2 kHz is selected, whereas the voltage controller bandwidth is kept as 12 Hz, which is, however, adjustable with the selection of controller coefficients. The decoupling matrix is calculated while considering up to 5th order harmonic and the parameters are obtained online based on the converter operating point.

To benchmark the contribution of the GHA based decoupler formation over the FHA based design, two experimental load transient results at different loading conditions are depicted in Figs. 13 and 14 comparing both strategies. For both the decoupler based control systems, the PI controller coefficients are optimally tuned for the best performance, i.e., least overshoot and settling time. This ensures a fair comparison between the two decoupling strategies. During the light load experiment, presented in Fig. 13, the converter is delivering a constant 22W at the 3rd output port at a voltage level of 22V, while the secondary output is being regulated at 114 V. A 80% load transient is provided to the 2nd output port by controlling the electronic dc load connected at the output side. The results show that under application of FHA based decoupled control the secondary port dc link experiences a voltage dip of 2V when the output load current increases, whereas it becomes 1.8V under the GHA based control. The observed effect of the same load transient on the 3rd port is a voltage dip of 0.5V and 0.3V under the FHA and GHA based decoupling actions, respectively. The settling time of the voltage transient on 3rd port is similar in both the cases. Thus, it can be concluded that with the implemented GHA based decoupler network, the dynamic performance of the converter has gained an improvement of 40% in terms of voltage overshoot.

Further, in order to observe a more prominent difference in control dynamics between the two decoupling actions, a load transient experiment is carried out in the developed TAB converter at a higher load condition that is depicted in Fig. 14. Here, the port-2 of the converter that is connected to a 120V dc link, is undergoing a load transient from 60W to 500W while the port-3 is supporting a constant dc load of 400W at 20V output. It can be clearly observed from the results that the output voltage at port-2 experiences a similar dip of 9V due to increased load demand under the influence of both the FHA and GHA based decouplers. However, the port-3 output voltage observes a dip of 1.4V with applied

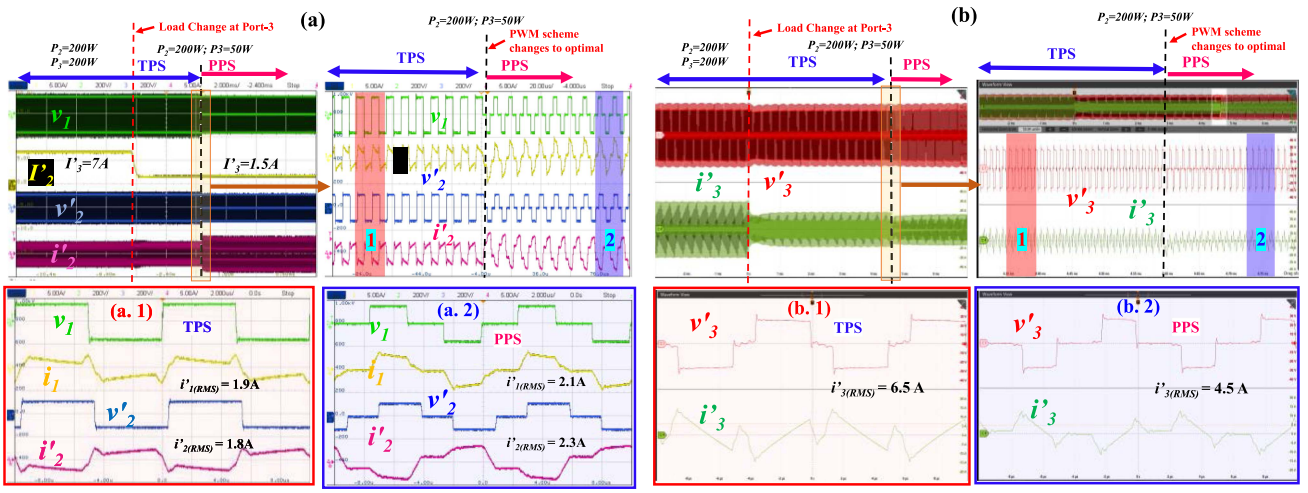

FIGURE 15. Experimental TAB waveforms under load transient at Port-3 (200 W to 50 W) under 160 V to 115 V (200 W, port-2) and 28 V(port-3) conversion, showcasing optimal duty cycle control: (a) Primary and Secondary bridge circuit voltage and current waveforms; (b) Tertiary bridge voltage and current waveforms. Zoomed in waveforms before and after optimal duty cycle transition (which occurs 5 ms after the load transient) are shown in (a.1) to (a.2) and (b.1) to (b.2). Scale for waveforms (b): i'_3 (ch 4, dc coupled): 10 A/div; v'_3 (ch 3, dc coupled): 10 V/div.

FHA based decoupled control whereas it only sees a 0.4V dip in case of proposed GHA oriented decoupling action, implying a 3.5 folds reduction in overshoot. Also, the proposed decoupler helps to lower settling time of the port-3 voltage by three folds compared to the existing decoupling strategy.

Furthermore, verifying the capability of the implemented control algorithm to track the optimized duty cycle operation under any output load or voltage variation, an experimental result is taken under 75% load change at port 3. The waveforms presented in Fig. 15 indicate that the converter was operating in steady state under TPS [5] modulation (employing $\varphi_2, \varphi_3, \delta_3$) scheme before the load change. Following the load step-down event at port-3 ($P_3 = 50$ W), the converter still operates in the same PWM mode without changing the operating duty cycles, while the output voltages are tracked by the implemented decoupled PI loops. Owing to the decoupled control, although there is a limited disturbance observed in port-3 dc link voltage (can be seen from peak voltage of the bridge voltage, v'_3) due to the load transient, the port-2 dc link voltage stays constant at 120V. After 4.5ms following the load transient event, the optimal duty tracking control block inside the controller updates the operating duty cycles (by incorporating all the optimal duty variables $\delta_1, \delta_2, \delta_3$, i.e., PPS [5]) minimizing the losses in the switching network. Comparing the zoomed-in results presented in (a.1-a.2) and (b.1-b.2), it can be observed that the port-3 RMS current, and all the switching current peaks have decreased considerably after the application of modified duty cycle parameters. Under the above-mentioned operating condition, this hybrid phase-duty controlled TAB achieves a 3.4% better TAB power stage efficiency than the conventional phase modulated control. Thus, it is validated from these results that the proposed control strategy facilitates the online dynamic tracking of the optimized control variables and hence minimized switching network losses in a TAB.

VI. CONCLUSION

This work showcases the theoretical modeling for any phase-duty controlled converter under the MAB family utilizing a frequency-domain GHA technique that circumvents the complex time domain based operating mode dependent formulations of winding currents and port-voltages. Moreover, a detailed GHA-based precise full order model of a TAB converter is derived while considering higher order harmonics into calculation in order to attain adequately superior steady state model accuracy. The comparison with the experimental steady state data demonstrates a 5% better accuracy in estimating the output port voltage by employing the GHA based full order model compared to the FHA based modeling approach. Furthermore, in order to precisely synthesize a decoupler network that decouples the power flow in a TAB converter, a reduced order phase-duty controlled TAB plant transfer function model is precisely synthesized by including higher order harmonics of the bridge voltages and currents into calculation. The load transient simulation result validates that the GHA based formulation of the decoupler network helps achieving 23% less overshoot compared to the FHA based decoupler implementation. Further, the experimental step-up load transient result benchmarks the reduction in overshoot and setting time by 3 and 3.5 folds, respectively, under the influence of implemented GHA oriented decoupler compared to the FHA based decoupling action. Moreover, it is experimentally validated that the proposed phase-duty optimal decoupled control helps reducing the total winding current RMS by 31% over the state-of-the-art leakage inductance minimized hardware based decoupling method; hence, achieving a 3.4% better TAB power stage efficiency.

APPENDIX

$$X = \begin{bmatrix} v_{o2} \\ v_{o3} \\ i_{12_{kR}} \\ i_{12_{kI}} \\ i_{13_{kR}} \\ i_{13_{kI}} \\ i_{23_{kR}} \\ i_{23_{kI}} \end{bmatrix};$$

$$A = \begin{bmatrix} -\frac{1}{R_2C_2} & 0 & -\sum\frac{4d_{k2}\sin(k\varphi_2)}{k\pi C_2} & -\sum\frac{4d_{k2}\cos(k\varphi_2)}{\pi kC_2} & 0 & 0 & \sum\frac{4d_{k2}\sin(k\varphi_2)}{\pi kC_2} & \sum\frac{4d_{k2}\cos(k\varphi_2)}{\pi kC_2} \\ 0 & -\frac{1}{R_3C_3} & 0 & 0 & -\sum\frac{4d_{k3}\sin(k\varphi_3)}{\pi kC_3} & -\sum\frac{4d_{k3}\cos(k\varphi_3)}{\pi kC_3} & -\sum\frac{4d_{k3}\sin(k\varphi_3)}{\pi kC_3} & -\sum\frac{4d_{k3}cos(k\varphi_3)}{\pi kC_3} \\ \frac{2d_{k2}\sin(k\varphi_2)}{\pi kL_{12}} & 0 & -\frac{R_{12}}{L_{12}} & k\omega_s & 0 & 0 & 0 & 0 \\ \frac{2d_{k2}\cos(k\varphi_2)}{\pi kL_{12}} & 0 & -k\omega_s & -\frac{R_{12}}{L_{12}} & 0 & 0 & 0 & 0 \\ 0 & \frac{2d_{k3}\sin(k\varphi_3)}{\pi kL_{13}} & 0 & 0 & -\frac{R_{13}}{L_{13}} & k\omega_s & 0 & 0 \\ 0 & \frac{2d_{k3}\cos(k\varphi_3)}{\pi kL_{13}} & 0 & 0 & -k\omega_s & -\frac{R_{13}}{L_{13}} & 0 & 0 \\ -\frac{2d_{k2}\sin(k\varphi_2)}{\pi kL_{23}} & \frac{2d_{k3}\sin(k\varphi_3)}{\pi kL_{23}} & 0 & 0 & 0 & 0 & -\frac{R_{23}}{L_{23}} & k\omega_s \\ -\frac{2d_{k2}\cos(k\varphi_2)}{\pi kL_{23}} & \frac{2d_{k3}\cos(k\varphi_3)}{\pi kL_{23}} & 0 & 0 & 0 & 0 & -k\omega_s & -\frac{R_{23}}{L_{23}} \end{bmatrix}$$

$$d_{k2} = \cos(k\delta_2);\ d_{k3} = \cos(k\delta_3).$$

$$M = \begin{bmatrix} 0 & -\frac{1}{C_2} & 0 \\ 0 & 0 & -\frac{1}{C_3} \\ 0 & 0 & 0 \\ -\frac{2\cos(k\delta_1)}{\pi kL_{12}} & 0 & 0 \\ 0 & 0 & 0 \\ -\frac{2\cos(k\delta_1)}{\pi kL_{13}} & 0 & 0 \\ 0 & 0 & 0 \\ 0 & 0 & 0 \end{bmatrix};\ N = \begin{bmatrix} v_{in} \\ I_{N,2} \\ I_{N,3} \end{bmatrix} B = \begin{bmatrix} -\sum\frac{4d_{k2}}{\pi C_2}\{i_{2_{kR}}\cos(k\varphi_2) \\ -i_{2_{kI}}sin(k\varphi_2)\} & 0 \\ 0 & -\sum\frac{4d_{k2}}{\pi C_3}\{i_{3_{kR}}\cos(k\varphi_3) \\ & -i_{3_{kI}}sin(k\varphi_3)\} \\ \frac{2V_2d_{k2}\cos(k\varphi_2)}{\pi L_{12}} & 0 \\ \frac{2V_2d_2\sin(\varphi_2)}{\pi L_{12}} & 0 \\ 0 & \frac{2V_3d_{k3}\cos(k\varphi_3)}{\pi L_{13}} \\ 0 & -\frac{2V_3d_{k3}\sin(k\varphi_3)}{\pi L_{13}} \\ -\frac{2V_2d_{k2}\cos(k\varphi_2)}{\pi L_{23}} & \frac{2V_3d_{k3}\cos(k\varphi_3)}{\pi L_{23}} \\ \frac{2V_2d_{k2}\sin(k\varphi_2)}{\pi L_{23}} & -\frac{2V_3d_{k3}\sin(k\varphi_3)}{\pi L_{23}} \end{bmatrix};\ \varphi = \begin{bmatrix} \Delta\varphi_2 \\ \Delta\varphi_3 \end{bmatrix}$$

$$x = \begin{bmatrix} \Delta v_{o2} \\ \Delta v_{o3} \\ \Delta i_{12_{kR}} \\ \Delta i_{12_{kI}} \\ \Delta i_{13_{kR}} \\ \Delta i_{13_{kI}} \\ \Delta i_{23_{kR}} \\ \Delta i_{23_{kI}} \end{bmatrix};$$

$$A' = \begin{bmatrix} -\frac{1}{R_2C_2} & 0 & -\sum\frac{4d_{k2}\sin(k\varphi_2)}{k\pi C_2} & -\sum\frac{4d_{k2}\cos(k\varphi_2)}{\pi kC_2} & 0 & 0 & \sum\frac{4d_{k2}\sin(k\varphi_2)}{\pi kC_2} & \sum\frac{4d_{k2}\cos(k\varphi_2)}{\pi kC_2} \\ 0 & -\frac{1}{R_3C_3} & 0 & 0 & -\sum\frac{4d_{k3}\sin(k\varphi_3)}{\pi kC_3} & -\sum\frac{4d_{k3}\cos(k\varphi_3)}{\pi kC_3} & -\sum\frac{4d_{k3}\sin(k\varphi_3)}{\pi kC_3} & -\sum\frac{4d_{k3}cos(k\varphi_3)}{\pi kC_3} \\ \frac{2d_{k2}\sin(k\varphi_2)}{\pi kL_{12}} & 0 & -\frac{R_{12}}{L_{12}} & k\omega_s & 0 & 0 & 0 & 0 \\ \frac{2d_{k2}\cos(k\varphi_2)}{\pi kL_{12}} & 0 & -k\omega_s & -\frac{R_{12}}{L_{12}} & 0 & 0 & 0 & 0 \\ 0 & \frac{2d_{k3}\sin(k\varphi_3)}{\pi kL_{13}} & 0 & 0 & -\frac{R_{13}}{L_{13}} & k\omega_s & 0 & 0 \\ 0 & \frac{2d_{k3}\cos(k\varphi_3)}{\pi kL_{13}} & 0 & 0 & -k\omega_s & -\frac{R_{13}}{L_{13}} & 0 & 0 \\ -\frac{2d_{k2}\sin(k\varphi_2)}{\pi kL_{23}} & \frac{2d_{k3}\sin(k\varphi_3)}{\pi kL_{23}} & 0 & 0 & 0 & 0 & -\frac{R_{23}}{L_{23}} & k\omega_s \\ -\frac{2d_{k2}\cos(k\varphi_2)}{\pi kL_{23}} & \frac{2d_{k3}\cos(k\varphi_3)}{\pi kL_{23}} & 0 & 0 & 0 & 0 & -k\omega_s & -\frac{R_{23}}{L_{23}} \end{bmatrix}$$

REFERENCES

[1] R. Hassan and G. Radman, "Survey on Smart grid," in *Proc. IEEE SoutheastCon*, 2010, pp. 210–213, doi: 10.1109/SECON.2010.5453886.

[2] M. Rashidi, N. N. Altin, S. S. Ozdemir, A. Bani-Ahmed, and A. Nasiri, "Design and development of a high-frequency multi-port solid-state transformer with decoupled control scheme," *IEEE Trans. Ind. Appl.*, vol. 55, no. 6, pp. 7515–7526, Nov./Dec. 2019, doi: 10.1109/TIA.2019.2939741.

[3] H. Tao, A. Kotsopoulos, J. L. Duarte, and M. A. M. Hendrix, "Family of multiport bidirectional DC–DC converters'," *IEE Proc. - Electric Power Appl.*, vol. 153, no. 3, pp. 451–458, 2006, doi: 10.1049/ip-epa:2005036.

[4] S. Dey and A. Mallik, "Multivariable-modulation-based conduction loss minimization in a Triple-active-bridge converter," *IEEE Trans. Power Electron.*, vol. 37, no. 6, pp. 6599–6612, Jun. 2022, doi: 10.1109/TPEL.2022.3141334.

[5] S. Dey, A. Mallik, and A. Akturk, "Investigation of ZVS criteria and optimization of switching loss in a triple Active bridge converter using Penta-Phase-Shift Modulation," *IEEE J. Emerg. Sel. Topics Power Electron.*, vol. 10, no. 6, pp. 7014–7028, Dec. 2022, doi: 10.1109/JESTPE.2022.3191987.

[6] S. Falcones, R. Ayyanar, and X. Mao, "A DC–DC multiport-converter-based solid-State transformer integrating distributed generation and storage," *IEEE Trans. Power Electron.*, vol. 28, no. 5, pp. 2192–2203, May 2013, doi: 10.1109/TPEL.2012.2215965.

[7] M. Jafari, Z. Malekjamshidi, and J. Zhu, "Design, analysis and control of a magnetically-coupled multi-port multi-operation-mode residential micro-grid," in *Proc. 20th Int. Conf. Elect. Mach. Syst.*, 2017, pp. 1–6, doi: 10.1109/ICEMS.2017.8056449.

[8] H. Chen, Z. Hu, H. Luo, J. Qin, R. Rajagopal, and H. Zhang, "Design and planning of a multiple-charger multiple-port charging system for PEV charging station," *IEEE Trans. Smart Grid*, vol. 10, no. 1, pp. 173–183, Jan. 2019, doi: 10.1109/TSG.2017.2735636.

[9] J. Schäfer, D. Bortis, and J. W. Kolar, "Multi-port multi-cell DC/DC converter topology for electric vehicle's power distribution networks," in *Proc. IEEE 18th Workshop Control Model. Power Electron*, 2017, pp. 1–9, doi: 10.1109/COMPEL.2017.8013326.

[10] G. Buticchi, L. F. Costa, D. Barater, M. Liserre, and E. D. Amarillo, "A quadruple active bridge converter for the storage integration on the more electric aircraft," *IEEE Trans. Power Electron.*, vol. 33, no. 9, pp. 8174–8186, Sep. 2018, doi: 10.1109/TPEL.2017.2781258.

[11] L. Wang, Z. Wang, and H. Li, "Asymmetrical duty cycle control and decoupled power flow design of a three-port bidirectional DC-DC converter for fuel cell vehicle application," *IEEE Trans. Power Electron.*, vol. 27, no. 2, pp. 891–904, Feb. 2012.

[12] C. Zhao, S. D. Round, and J. W. Kolar, "An isolated three-port bidirectional DC–DC converter with decoupled power flow management," *IEEE Trans. Power Electron.*, vol. 23, no. 5, pp. 2443–2453, Sep. 2008, doi: 10.1109/TPEL.2008.2002056.

[13] Y. Chen, P. Wang, H. Li, and M. Chen, "Power flow control in multi-active-bridge converters: Theories and applications," in *Proc. IEEE Appl. Power Electron. Conf. Expo.*, 2019, pp. 1500–1507, doi: 10.1109/APEC.2019.8722122.

[14] S. Bandyopadhyay, P. Purgat, Z. Qin, and P. Bauer, "A multiactive bridge converter with inherently decoupled power flows," *IEEE Trans. Power Electron.*, vol. 36, no. 2, pp. 2231–2245, Feb. 2021, doi: 10.1109/TPEL.2020.3006266.

[15] P. Wang, X. Lu, W. Wang, and D. Xu, "Hardware decoupling and autonomous control of series-resonance-based three-port converters in DC microgrids," *IEEE Trans. Ind. Appl.*, vol. 55, no. 4, pp. 3901–3914, Jul./Aug. 2019, doi: 10.1109/TIA.2019.2906112.

[16] O. M. Hebala, A. A. Aboushady, K. H. Ahmed, and I. Abdelsalam, "Generalized active power flow controller for multiactive bridge DC–DC converters with minimum-current-point-tracking algorithm," *IEEE Trans. Ind. Electron.*, vol. 69, no. 4, pp. 3764–3775, Apr. 2022, doi: 10.1109/TIE.2021.3071681.

[17] T. Liu et al., "Design and implementation of high efficiency control scheme of dual active bridge based 10 kV/1 MW solid state transformer for PV application," *IEEE Trans. Power Electron.*, vol. 34, no. 5, pp. 4223–4238, May 2019, doi: 10.1109/TPEL.2018.2864657.

[18] S. R. Sanders, J. M. Noworolski, X. Z. Liu, and G. C. Verghese, "Generalized averaging method for power conversion circuits," *IEEE Trans. Power Electron.*, vol. 6, no. 2, pp. 251–259, Apr. 1991, doi: 10.1109/63.76811.

[19] C. Darmody, S. Dey, A. Mallik, and A. Akturk, "Online optimization of the triple-active-bridge converter control parameters for maximum efficiency point tracking," in *Proc. IEEE 1st Ind. Electron. Soc. Annu. On-Line Conf.*, kharagpur, India, 2022, pp. 1–6, doi: 10.1109/ONCON56984.2022.10126742.

[20] "Battery selection practice for aerospace power systems," MSFC to NASA, Washington, DC, USA, Feb. 1999.

SAIKAT DEY (Graduate Student Member, IEEE) received the B.Tech. degree in electrical engineering from the Indian Institute of Engineering Science and Technology, Shibpur, India, in 2018. He is currently working toward the Ph.D. degree in Systems Engineering with Arizona State University, Polytechnic Campus, Mesa, AZ, USA. From 2018 to 2020, he was a Power Electronics Design Engineer with Tagore Technology, India Centre, where he developed some highly efficient and compact power electronic converter solutions with Tagore's GaN power products. In 2023, he was Power Conversion Control Intern with Lucid Motors, where he was with the Vehicle Charging team. His main research interests include the design, control, and optimization of multi-port dc-dc power electronic converters solutions using wide-bandgap semiconductors.

While in school, he has earned various awards and recognitions, including the IEEE TPEL Prize Paper Award in 2023, TSMC AZ Fellowship in 2023, Honorary Mention in Link Energy Fellowship in 2023, IEEE IES HOPE Prize in 2022, Outstanding Mentor Award in 2022, University Graduate Fellowship in 2021, Outstanding Research Award in 2021 at ASU, and Best Bachelors' Thesis Award from the Indian National Academy of Engineering in 2018.

AYAN MALLIK (Senior Member, IEEE) received the M.S. and Ph.D. degrees in electrical engineering from the University of Maryland, College Park, MD, USA, in 2018 and 2019, respectively. In August 2019, he joined Arizona State University, Tempe, AZ, USA, as an Assistant Professor. He is an author or coauthor of more than 80 peer-reviewed publications and four issued/pending U.S. Patents. His research interests include the design, control and multi-objective optimization of power electronic converters, highly efficient and high-density power conversion solutions in the applications of more-electric-aircrafts, electric vehicles, renewables, extreme environment space, wireless charging, and data centers. Dr. Mallik was the recipient of various awards and recognitions, including National Science Foundation CAREER Award in 2023, IEEE Transactions on Power Electronics (TPEL)-2022 Prize Paper Award, first place in Help Others ProgrammE competition organized by IEEE Industrial Electronics Society, first place in Dean's Doctoral Dissertation award competition at UMD in 2019, ECE distinguished dissertation award at UMD in 2019, University of Maryland's (UMD) Invention of the Year award in 2018, Jimmy H.C. Lin invention award in 2018, and third place in Allegheny Region Cleantech University Prize Collegiate Competition in 2017 sponsored by DOE.